Twisting Bilayer Graphene Superlattices

Chun-Chieh Lu,[†] Yung-Chang Lin,[†] Zheng Liu,[‡] Chao-Hui Yeh,[†] Kazu Suenaga,[‡] and Po-Wen Chiu[†,*]

[†]Department of Electrical Engineering, National Tsing Hua University, Hsinchu 30013, Taiwan, and [‡]National Institute of Advanced Industrial Science and Technology (AIST), Tsukuba 305-8565, Japan

ABSTRACT Bilayer graphene is an intriguing material in that its electronic structure can be altered by changing the stacking order or the relative twist angle, yielding a new class of low-dimensional carbon system. Twisted bilayer graphene can be obtained by (i) thermal decomposition of SiC; (ii) chemical vapor deposition (CVD) on metal catalysts; (iii) folding graphene; or (iv) stacking graphene layers one atop the other, the latter of which suffers from interlayer contamination. Existing synthesis protocols, however, usually result in graphene with polycrystalline structures. The present study investigates bilayer graphene grown by ambient pressure CVD on polycrystalline Cu. Controlling the nucleation in early stage growth allows the constituent layers to form single hexagonal crystals. New Raman active modes are shown to result from the twist, with the angle determined by transmission electron microscopy. The successful growth of single-crystal bilayer graphene provides an attractive jumping-off point for systematic studies of interlayer coupling in misoriented few-layer graphene systems with well-defined geometry.

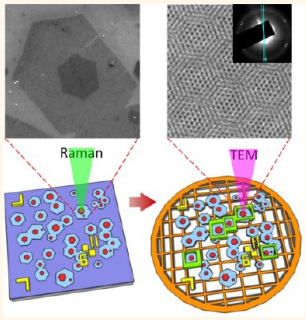

KEYWORDS: twisted bilayer graphene · single crystal · Raman · TEM

Graphene is a single atomic layer of carbon crystal which exhibits remarkable electronic properties as a result of its particular conical band structures with a Dirac-type spectrum of low-energy quasiparticles.[1] It provides an unique platform to enrich our understanding in condensed-matter phenomena that are experimentally not observable in conventional two-dimensional electron gases[2,3] and also points to a broad range of applications based on its electronic structure and transport properties.[4−7] Aside from the peculiar massless Dirac fermions that emerge in single-layer graphene (SLG), stacking graphene sheets one atop the other may result in very different energy-momentum relations,[8−10] expanding the electronic versatility of this two-dimensional carbon system. In the simplest architecture, two graphene layers can be arranged in an AA, AB, or a twisted configuration; the physical properties of such bilayer graphene (BLG) are correlated with the stacking order and relative twist angle,[9−12] with each type possessing a unique π-electron landscape. For example, the breaking of inversion symmetry in AB stacked BLG leads to a quadratic energy dispersion with a band gap tunable by a perpendicular electric field.[13−15] For twisted (rotationally stacking-faulted) BLG, the electronic properties critically depend upon the twist angle, as revealed by measurements combing scanning tunneling microscopy and Landau-level spectroscopy: the electronic properties of the twisted BLG with an angle >20° are indistinguishable from that of SLG, while a substantial reduction of Fermi velocity occurs for small angles.[16,17]

The early studies of the rotational stacking fault have been focused on SiC-derived graphene which is of high quality, but suffers from a strong substrate interaction.[18,19] To study the Raman properties of twisted BLG, folded or consecutively transferred graphene layers are used.[20,21] In these cases, the existence of interlayer contamination decisively affects on exploring intrinsic properties of the coupled two layers.[22,23] Therefore, chemical vapor deposition (CVD) synthesis of single-crystal twisted BLG that can be isolated from their growing substrate would produce a material of fundamental interest. Recently, high-quality graphene growth has been realized on various transition metals using CVD.[24−26] The most noticeable demonstration is the scalable growth of fewer graphene layers on Cu.[27] At low growth pressure, the CVD process can be surface-mediated and somewhat self-limiting due to the negligible solubility of carbon in Cu, yielding predominantly SLG typically made of randomly oriented domains. Single-crystal

* Address correspondence to pwchiu@ee.nthu.edu.tw.

Received for review December 25, 2012 and accepted February 28, 2013.

Published online February 28, 2013
10.1021/nn3059828

© 2013 American Chemical Society

graphene with lateral dimensions of up to several millimeters has been realized by controlling carbon nucleation in the self-limiting reaction.[28−30] These results have inspired the search for a new protocol that allows the CVD growth of two single-crystal graphene layers coupled at a separation of only van der Waals distance. Recently, it has been reported that self-limiting growth can be broken using modified CVD conditions (*e.g.*, high growth pressure and enlarged supply of carbon feedstock), yielding multiple stacks of graphene layers on Cu.[31,32] This paper studies BLG grown in the early stages of ambient pressure CVD (AP-CVD). Controlling the nucleation conditions on Cu foils allows both constituent layers to form as hexagonal single crystals. Each BLG grain possesses a specific twist angle which is characterized by Raman spectroscopy in combination with transmission electron microscopy (TEM). This combined technique provides the one-to-one correlation between the twist angle and Raman properties.

RESULTS AND DISCUSSION

Figure 1 shows the scanning electron microscopy (SEM) images of a BLG array and magnified individual grains on Si substrates. Each grain consists of two graphene layers, with the small (secondary) and large (primary) layers typically measuring 3−5 and 10−15 μm, respectively. Each layer has a prominent hexagonal morphology that persists without apparent interruption by Cu surface imperfections, indicating their single crystalline nature.[29,33,34] Their edges are predominantly oriented parallel to the zigzag direction, as will be detailed in the Raman mappings and also in the TEM imaging (Supporting Information). The secondary hexagon may be elongated along one of the zigzag directions, as shown in Figure 1c. In some cases, multiple nucleation of secondary grains on the host layer can be observed, with small satellite grains arranged around the central grain (Figure 1c, Supporting Information). Over a prolonged growth time, a third layer is seen to start nucleating from the center of the existing BLG (Figure 1d). This implies that the early embryos act as a preferential site for the later growth of a new layer, and a proper control over the embryo size might be of importance in the layer-by-layer stacking single crystal graphene.

Controlled growth of single-crystal BLG grains and arrays were achieved by optimizing a number of growth parameters. Critical factors include temperature, hydrogen partial pressure, methane concentration, and copper surface conditions, all of which are mutually correlated and may affect the growth and nucleation of the primary and secondary layers.[35,36] Figure 2 shows the SEM images of the morphology changes given changes to these parameters. Temperature plays a key role in the nucleation rate and needs to be addressed prior to the systematic search for an optimized growth protocol. As shown in Figure 2a, a lower temperature (950 °C) favors the growth of polycrystalline bilayer graphene

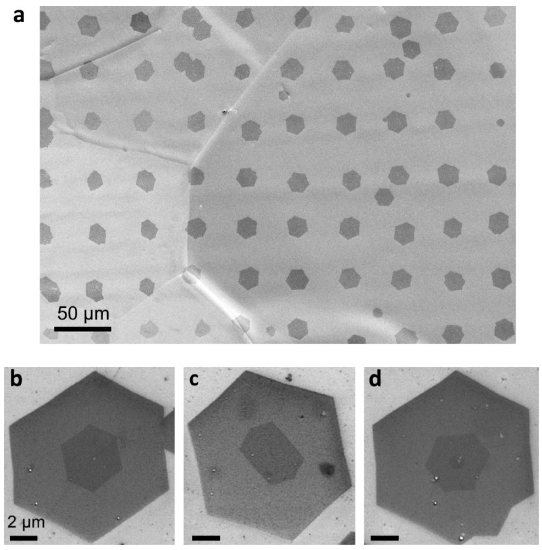

Figure 1. CVD single-crystal BLG. (a) SEM image of bilayer graphene array. An array of carbon seeds comprising cross-linked PMMA by a strong electron-beam irradiation was made on Cu foil prior to the growth of BLG, followed by the AP-CVD growth using the optimized parameters shown in the Methods section. The period of the array is 50 μm, and the size of each seed is ~1 μm. Few grains that nucleated randomly are also observed. (b−d) Different orientation of the twisted BLG grains. In panel c, an elongation of the secondary layer along one of the zigzag directions is obvious. Small satellite grains on the primary layer can sometimes be seen near the secondary grain in panel d. Figure 1d shows a third grain which starts nucleating at the center of the BLG grains in a prolonged growth time. The figures in (b−d) share the same scale bar.

with an arbitrary grain shape, while increased temperatures result in the shrinkage of the secondary layer. At 1050 °C, hexagonal embryos form which then develop into graphene dendrites at a low hydrogen partial pressure (5 Torr), but into star-shaped graphene at an increasing partial pressure (>13 Torr), with a secondary grain nucleated preferentially at the center of the host layer (Figure 2b). From this point on, methane concentration becomes critical to further manipulate the growth of the secondary layer, which tends to vanish at a low methane concentration (<50 ppm, Figure 2c). Increasing the methane concentration to 80 ppm results in stable BLG growth with both layers being single crystal in nature. Further increasing the methane concentration has little impact on the hexagonal morphology, but does affect the lateral dimensions of the layers. A blurry concentration region, which is relevant to other gas flows and typically covers spans between 40 and 70 ppm in our growth conditions, exists for the cogrowth of single- and bilayer graphene grains. In addition to the temperature and gas effects, the growth of single-crystal BLG is also largely influenced by Cu foils with different crystalline purities, surface roughness, and foil thickness (Figure 2d). Under optimized growth conditions, the largest secondary layer is 5−6 μm prior to coalescing into films.

At a microscopic scale, the crystallographic edges of thus grown graphene are not ideally straight,

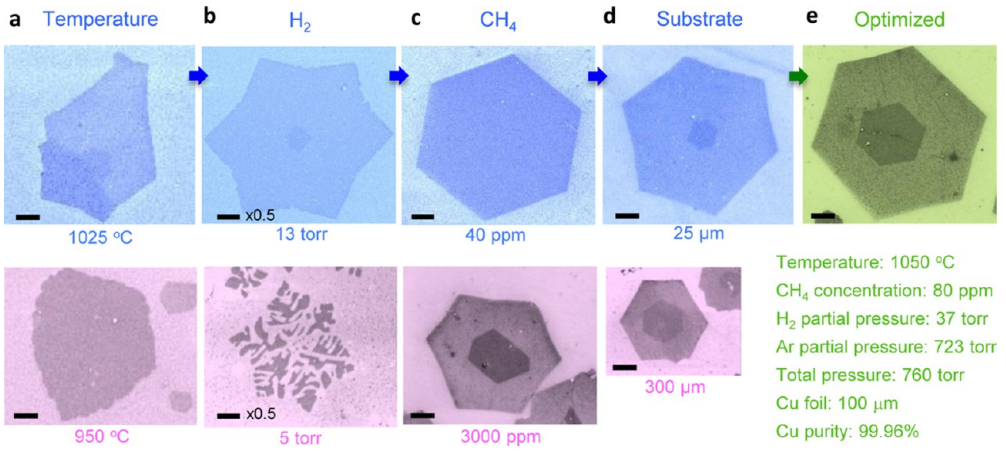

Figure 2. Tuning CVD growth for single-crystal BLG. (a−d) Representative SEM images of graphene grown using the parameters provided in the Methods section. Only the indicated parameters are varied in the growth process: (a) temperature effect; (b) hydrogen partial pressure; (c) methane concentration; (d) Cu thickness. (e) SEM image of single-crystal BLG with optimized growth conditions.

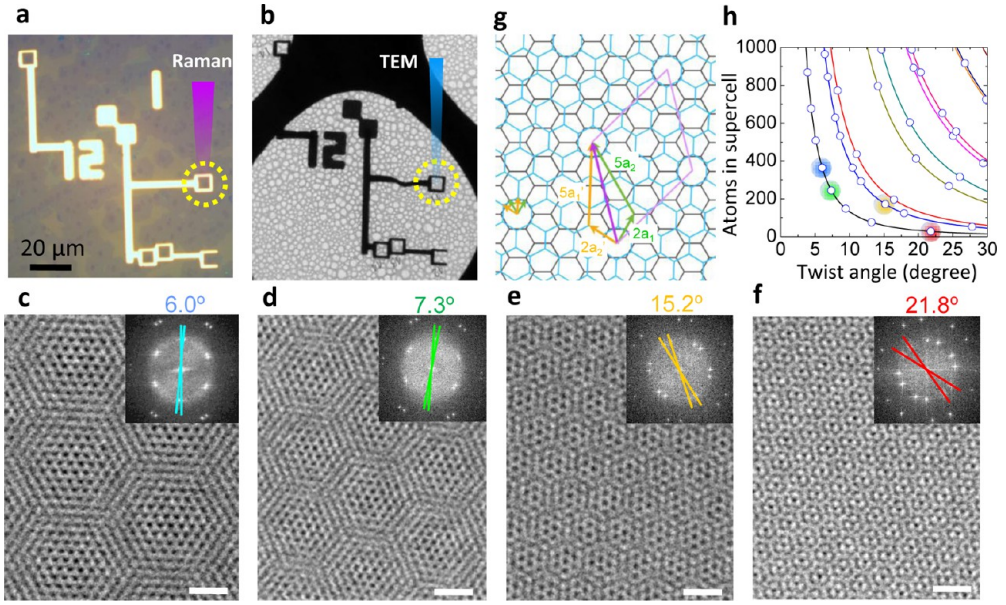

Figure 3. TEM images and supercells of twisted BLG. (a) Optical photograph of BLG grains transferred onto a Si substrate, with coordinate markers and scaffolds that encircle the grains for Raman measurements and later for TEM imaging and SAED. (b) Low-resolution TEM image of the same structure transferred onto a Cu grid. (c−f) HR-TEM images of BLG with different twist angles. Moiré patterns are formed due to the misorientation of the two layers. The insets for each figure present the fast Fourier transform patterns. All the scale bars are 1 nm. (g) Schematic of a commensurate twist of two graphene layers. The twist angle θ leads to a large supercell defined by the purple rhombus. A twist vector $\mathbf{T} = m\mathbf{a}_1 + n\mathbf{a}_2$, where $\mathbf{a}_1 = a(\sqrt{3}/2, 1/2)$ and $\mathbf{a}_2 = a(\sqrt{3}/2, -1/2)$ are the primitive lattice vectors for the first graphene layer, is used to characterize the periodic structure of a twisted BLG. n and m are integers ($0 < m < n$) such that $\gcd(n, m) = 1$. (h) Angle-dependent number of C atoms in the supercell of a commensurate twist. The marked points denote the commensurate twists of the HR-TEM images shown in panels c−f.

irrespective of the stacking order and twist angle (see Supporting Information). Nonetheless, the edges provide a rude method to determine the twist angle between the two layers. Precisely correlating the Raman spectra with the twist angles requires differentiating AA from AB stacking and identifying angles close to 0 or 30° through selected area electron diffraction (SAED). To achieve this, gold markers were first patterned around the BLG by standard e-beam lithography, followed by a clean transfer of the marker/graphene to a Cu grid using the previously reported techniques.[22,23] Figure 3 panels a and b respectively show optical photographs of the marker/graphene on Si substrate and a low-resolution TEM image of the same structure transferred onto a Cu grid. This method inevitably results in *ca.* 40−50% of BLG loss due to the blockage of BLG by metal grids. Figure 3 panels c−f show high-resolution TEM (HR-TEM) images of different graphene superlattices interpreted as Moiré patterns caused by misorientations between graphene layers. The insert in each figure presents the corresponding Fourier transform defractograms (FFTs), showing the twist angles. A crystal forms, as a matter of principle, only at a discrete set of commensurate twist angles

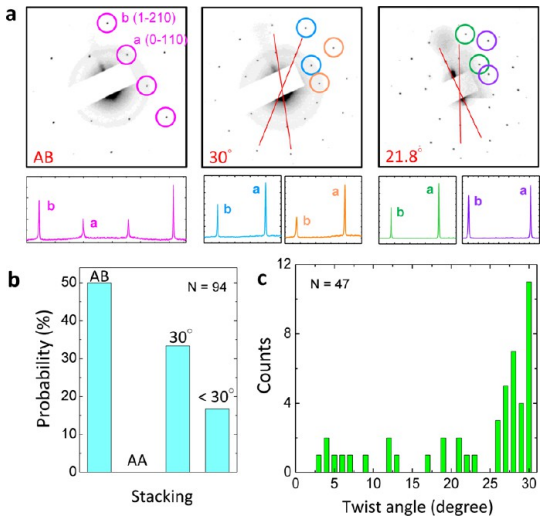

Figure 4. Electron diffractions and histograms of BLG. (a) Electron diffraction patterns of AB stacked, 30°, and 21.8° twisted BLG, with the spots labeled by Miller-Bravais indices. The lower panels show the corresponding spot intensities taken along the marked axes, *e.g.*, 1−210 to −2110 axis for the AB stacked BLG. The twisted BLG has intensity ratio of $I_a/I_b > 1$, a characteristic identical to that of SLG. (b) Histogram of the AB stacked, AA stacked, and twisted BLG for all the diffraction patterns collected. (c) Histogram of the twist angle for the twisted BLG.

when two graphene layers are overlaid. The size of the supercell varies greatly with a slight change to the angle (Figure 3g,h). However, the Moiré pattern observed in TEM might also be caused by an incommensurate stack which behaves as if it were commensurate. The difference between a commensurate angle and a neighboring incommensurate angle can be very small, often indistinguishable, especially for small angles.

To gain insight into the distribution of stacking orders and twist angles, more than 200 BLG samples were prepared and half were successfully examined by SAED after acquiring Raman spectra. Figure 4a shows the diffraction patterns of AB stacked, 30° twisted, and 21.8° twisted BLG. All the patterns exhibit 6-fold symmetry. For AB stacked BLG, the intensity ratio is $I_{\{1100\}}/I_{\{2100\}} < 1$, as opposed to $I_{\{1100\}}/I_{\{2100\}} > 1$ for SLG, consistent with other computational[37] as well as experimental[38] studies. For twisted BLG, however, the intensity ratio is always $I_{\{1100\}}/I_{\{2100\}} > 1$, resembling the case of SLG. Even for the 21.8° twisted BLG, which is constructed with the smallest commensurate supercell, the ratio remains above unity. Figure 4b presents our analysis of stacking probability, showing that 50% of the BLG are AB stacked, which is energetically most favorable in nature. The rest are twisted BLG. Surprisingly, our statistics showed no AA stacking (a translational shift of AB stacking). This shows a sharp contrast to the pyrolytic graphite whose BLG often exhibits AA stacking.[39] Further comparison shows that over 60% of the BLG have a twist angle $\theta > 25°$, as opposed to fewer than 10% for $\theta \leq 5°$, an angle at which the Fermi velocity is substantially reduced with respect to SLG.[16,40]

The relative orientations and interlayer coupling in twisted BLG have been intensively studied, both experimentally[12,16] and theoretically.[9,10] For example, an appreciable enhancement of the G band intensity for specific twist angles was attributed to the formation of a low-energy singularity in the joint density of states.[20,41,42] Two new Raman features also appear in the twisted BLG as a result of intravalley and intervalley double resonance processes involving elastic electron scattering by the static potential which stems from the interaction between the two layers. Previous studies could only be conducted in folded BLG with short-range atomic registry or in polycrystalline BLG with perturbation of other grain orientations.[43] The single-crystal twisted BLG studied here provides a clean system to gain more insight into the angle-dependent Raman properties. We performed Raman measurements using a scanning confocal setup with laser wavelengths of 488, 514, and 633 nm and intensity below 2 mW focused to a diffraction-limited spot size. The graphitic signal of single-crystal BLG, as shown in Figure 5a for different twist angles, appears at ∼1580 (G band). The absence of D band (∼1350 cm^{-1}) indicates the high crystallinity and low structural defects in the BLG. Careful comparison between the AB stacked and twisted BLG shows a prominent feature at the wavenumber 1625 cm^{-1} (called the R′ band) for twisted BLG with small angles.[21] This peak is nondispersive (Figure 5b) and has its intensity maximum at $\theta = 5°$ under red light excitation ($E_L = 1.96$ eV). The R′ intensity maximum shifts to larger angles as the laser energy increases. Although this unusual Raman feature occurs in the same spectral range as the D′ band of disordered sp^2 carbon, it cannot be assigned to the D′ band which exhibits a dispersion rate of ∼10 cm^{-1}/eV in the visible range and is associated with high defect densities.[44]

In light of Carozo's work,[21] this new Raman feature of twisted BLG can be interpreted in the framework of a double resonance process, as elucidated in Figure 5c in momentum space. Resembling the origin of the D′ band where the scattering of photoexcited electrons near the **K** (or **K**′) points is mediated by a phonon ω_q and a static disorder potential V_{-q}, the R′ band is attributed to a similar intravalley double resonance process with the static potential generated by the weak coupling of the two layers. The mismatch between the two layers gives rise to a reciprocal rotational vector **q**. When an electron−hole pair is created by a photon with energy E_L in one of the valleys located at the **K** (or **K**′) point of the Brillouin zone boundary, the electron is elastically scattered by the momentum **q** to another point of the same Dirac cone with the opposite wavevector $-\mathbf{k_0}$, thus creating a phonon with wavevector $\mathbf{Q}_{intra}$. The inelastic backscattering by the phonon returns the electron to $\mathbf{k_0}$ in the same valley where it completes its Raman roundtrip transition by recombining with its companion hole in the course of emitting Raman light of energy $\hbar\omega_s$. The **q** increases as increasing

θ, and this, in turn, requires a larger wavevector $\mathbf{k}_0$ of electrons to be excited by the laser energy E_L to proceed the intravalley double resonance. Therefore, θ and E_L have one-to-one correspondence. For a given θ, deviation of E_L from the specific energy $E_L(\theta)$ will suppress the R′ double resonance, thereby lowering the intensity of the peak (Figure 5b).

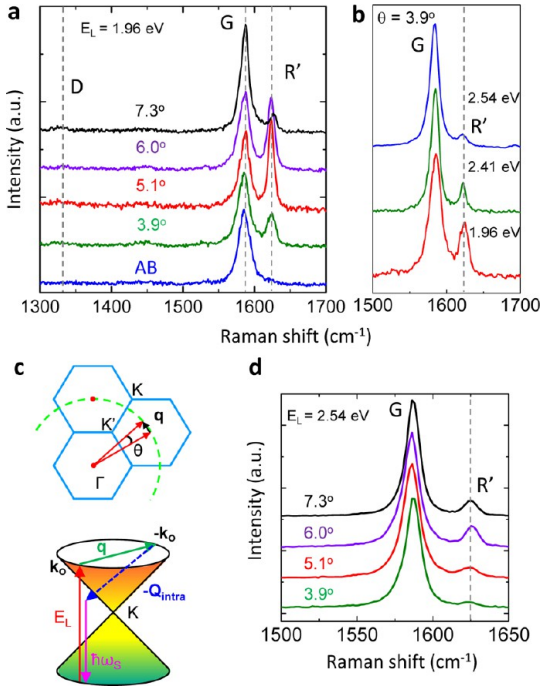

Figure 5. Raman spectra of twisted BLG with small angles. (a) Raman spectra in the range of 1300 and 1700 cm^{-1} for twist angles from 3.9 to 7.3°. The spectrum of AB stacked BLG is presented as reference. A new Raman active mode (R′ band), centered at 1625 cm^{-1}, appears in the twisted BLG. (b) Raman spectra in the vicinity of the R′ band for 3.9° twisted BLG taken at different laser excitation energies. (c) The upper panel shows the Brillouin zone of one layer, with a rotation of the other, yielding a rotation momentum q. The lower panel schematically illustrates an intravalley double-resonance process involving elastic electron scattering by the static potential. (d) Raman spectra in the range of 1500 and 1650 cm^{-1} for twist angles from 3.9 to 7.3°. The dashed lines in panels a–c are eye-guides for the Raman modes.

The R′ band is only activated at a low twist angle ($3° < \theta < 8°$) in the visible range and becomes inaccessible at a larger twist angle due to the large **q** vector which requires electrons with much higher energy to complete the intravalley double resonance process. The linear dependence of the R′ frequency ($\omega_{R'}$) with respect to the twist angle (θ) makes the $\omega_{R'}$ increasing monotonically as θ increases for $\theta < 9°$.[21] This results in a shift of R′ intensity maximum to a larger angle as E_L increases. Figure 5d shows the 488 nm-excited Raman spectra of the same twisted BLG shown in Figure 5b. We can clearly see that the R′ intensity maximum shifts from $\theta = 5.1°$ for $E_L = 1.96$ eV to $\theta = 6.0°$ for $E_L = 2.33$ eV. Moreover, the R′ intensity maximum becomes weaker as the twist angle increases, for example, $I_{R'}/I_G$ ($\theta = 5.1°$, $E_L = 1.96$ eV) = 1.22, $I_{R'}/I_G$ ($\theta = 6°$, $E_L = 2.33$ eV) = 0.20, and $I_{R'}/I_G$ ($\theta = 6°$, $E_L = 2.54$ eV) = 0.18.

Figure 6 shows the Raman mappings of AB stacked and 28° twisted BLG using a 488 nm excitation. The intensity maps convey important information on the geometrical and electronic structures of graphene. The G band associated with the zone-center in-plane stretching eigenmode reveals an sp^2 carbon–carbon bond, with an intensity proportional to the stacking numbers (<10 layers) due to the interference of the laser in the graphene layers as well as multireflections of Raman light.[45] As a result, the G band intensity in the bilayer region is always higher than that in the single layer region, irrespective of the stacking order or twist angle. For the 2D band, the intensity of the AB stacked bilayer is rather uniform, as compared with that of the

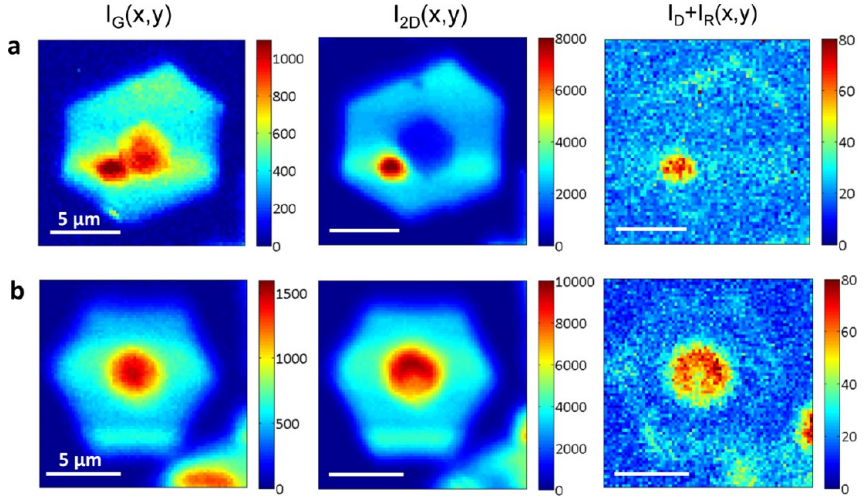

Figure 6. Two-dimensional Raman mappings of BLG. (a,b) Raman intensity maps for AB stacked and 28° twisted BLG using 488 nm excitation. The spectral regions of the intensity maps are G peak (1560–1610 cm^{-1}); 2D peak (2650–2750 cm^{-1}); and D and R peaks (1335–1385 cm^{-1}). A satellite BLG appears near the AB stacked BLG in panels a and shows properties similar to those of the 28° twisted BLG in panels b. All the maps have the same scale bar.

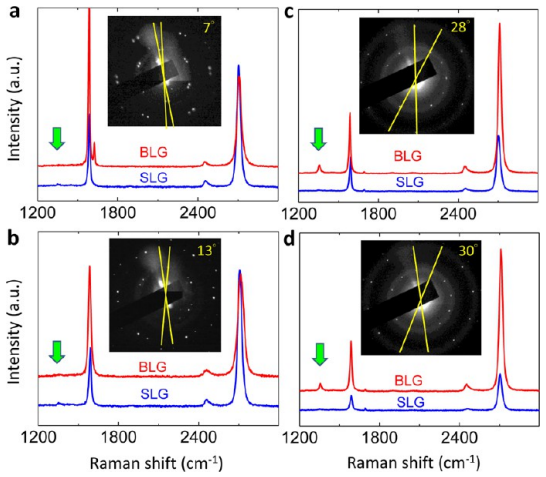

Figure 7. Full Raman spectra of BLG with each angle determined by electron diffraction. The spectra were taken using 488 nm excitation. The arrows point to the R peak region.

28° twisted bilayer, but with intensity in the AB stacked bilayer lower by a factor of 0.2−0.25 due to the lifting of band degeneracy that allows four possible pathways for phonon scattering.[46]

In all the Raman maps shown in Figure 6, the D band region is relatively featureless at the grain edges, indicating a zigzag termination which does not fulfill the momentum conservation in the elastic intervalley scattering of the electrons and holes and as a result cannot contribute to the Raman D band.[47] Unlike SiC-derived graphene, which prefers armchair termination,[48] our AP-CVD conditions yield predominantly zigzag edges, similar to other CVD graphene grown at low hydrocarbon concentrations.[33,34,49] For the BLG with a large twist angle ($\theta > 25°$), a new Raman active mode, weakly peaking at 1375 cm^{-1}, becomes accessible under blue light excitation (Figure 6b). Although this Raman feature occurs in the same spectral range as the D band of disordered sp^2 carbon, the D band is not a plausible cause, as revealed in the high crystalline quality of the bilayer region in the large-area TEM images with atomic resolution (Supporting Information). Consistent with the origin of the R′ band, this new Raman feature, called the R band, results from another double-resonance process activated by the same above-mentioned static potential. The photoexcited electron proceeds to an intervalley double resonance in which the electron is first elastically scattered by the large rotation momentum **q** (due to a large value of θ) to an inequivalent Dirac valley, followed by an inelastic backscattering by a zone boundary phonon $-\mathbf{Q}_{inter}$, which brings the electron back to $\mathbf{k}_0$ and recombines with its companion hole for Raman light emission.

The R peak is nondispersive and appears only at large angles in the visible range, as compared in Figure 7. It shows that a peak near 1375 cm^{-1} appears only in the bilayer regions with a large twist angle (28 or 30°), while it vanishes in the single-layer regions and the bilayer regions with a small twist angle (7 or 13°). Although one can use the nondispersive feature to differentiate it from the D peak, it cannot be activated by low energy light sources which are generally available in a lab. Excitation energies in the ultraviolet range are required to access this mode for the small twist angles.[21] Moreover, it is very unlikely that all the Raman mapped graphene areas contain low defects, except for the bilayer regions with a large twist angle. It is therefore rational to attribute this peak to the R peak, instead of the D peak. Further systematic study using continuous high excitation energies will help in understanding the angle-dependent Raman modes.

CONCLUSIONS

We have synthesized single-crystal bilayer graphene with different stacking orders and twist angles using AP-CVD under controlled nucleation conditions. The grown graphene layers are of high crystalline quality, as revealed in the featureless Raman D band and the high electron mobility (8000 $cm^2/V \cdot s$ shown in Supporting Information) without particular treatment of the silicon substrate surface. The rotationally faulted bilayers result in Moiré patterns in commensurate stacks. Each twist angle in the bilayer graphene, determined by electron diffraction, defines a particular electronic band structure which interprets the unusual Raman active modes as a result of the intra- or intervalley double resonance process in twisted stacking. Unlike the layer-by-layer stacking of transferred graphene, which causes unavoidable polymer contamination between the constituent layers, the electronic structure and transport properties of the CVD grown single-crystal bilayer graphene paves the way for a broad range of applications.

METHODS

Graphene Synthesis and Transfer. Optimized single-crystal BLG grains and arrays were grown by the AP-CVD of methane (99.99%) on polycrystalline Cu foils. Prior to growth, the Cu foils were cleaned by acetone and IPA with sonication, followed by etching in acetic acid for 30 min to remove surface oxides. The Cu foil was then mounted in the CVD chamber and the furnace was ramped up to 1050 °C over 40 min, with constant flows of 300 sccm Ar and 10 sccm H_2. After reaching 1050 °C, the sample was annealed for 90 min without changing the gas flow. For graphene growth, methane (80 ppm) mixed with the flows of 300 sccm Ar and of 15 sccm H_2 was fed into the reaction chamber for ~7 min to form bilayer graphene. Following the growth, the Cu foil was moved to the cooling zone under the protection of Ar and H_2. Some more details of our CVD conditions (*i.e.*, the carbon concentration *vs* time relationship) are provided in Supporting Information. For the transfer process, the graphene sheets were first coated with a thin layer of polycarbonate, followed by etching in HCl aqueous solution to remove the Cu. The polycarbonate film, along with the

attached graphene, was then transferred onto a silicon substrate. The polycarbonate film was then removed using chloroform. Same process was also used for second transfer onto a Cu grid for TEM observations.

Transmission Electron Microscopy. A field emission TEM JEM-2010F (JEOL) equipped with a CEOS post-specimen spherical aberration corrector (C_s corrector) was operated at 120 kV for the TEM observations. A Gatan 894 CCD camera was used for digital recording of the SAED patterns and HR-TEM images. A sequence of HR-TEM images (10 frames) was recorded, with 1 s exposure time for each. After drift compensation, some frames can be superimposed to increase the signal-to-noise (SN) ratio for display.

Raman Spectroscopy and Mapping. A high-resolution Micro Raman spectrometer (LabRaman 800, Horiba Jobin Yvon) equipped with a motorized sample stage was used to acquire the Raman spectra and spatial mapping. A 100× objective was used to provide a diffraction-limited spot size. Three different laser excitations were used: $\lambda = 488$, 514, and 633 nm. The power level was set below 1−2 mW to avoid heating or damage to the sample.

Conflict of Interest: The authors declare no competing financial interest.

Acknowledgment. Z.L. and K.S. acknowledge the support from JST Research Acceleration programme. The other authors acknowledge the support of the Taiwan National Science Council under Contract No. NSC 100-2112-M-007-014-MY3.

Supporting Information Available: Additional graphene characterizations, growth parameters, electrical transport, HR-TEM images, and Raman characterizations are given in Figures S1−S13. This material is available free of charge *via* the Internet at http://pubs.acs.org.

REFERENCES AND NOTES

1. Wallace, P. R. The Band Theory of Graphite. *Phys. Rev.* **1947**, *71*, 622–634.
2. Novoselov, K. S.; Geim, A. K.; Morozov, S. V.; Jiang, D.; Katsnelson, M. I.; Grigorieva, I. V.; Dubonos, S. V.; Firsov, A. A. Two-Dimensional Gas of Massless Dirac Fermions in Graphene. *Nature* **2005**, *438*, 197–200.
3. Geim, A. K.; Novoselov, K. S. The Rise of Graphene. *Nat. Mater.* **2007**, *6*, 183–191.
4. Morozov, S. V.; Novoselov, K. S.; Katsnelson, M. I.; Schedin, F.; Elias, D. C.; Jaszczak, J. A.; Geim, A. K. Giant Intrinsic Carrier Mobilities in Graphene and Its Bilayer. *Phys. Rev. Lett.* **2008**, *100*, 016602.
5. Castro Neto, A. H.; Guinea, F.; Peres, N. M. R.; Novoselov, K. S.; Geim, A. K. The Electronic Properties of Graphene. *Rev. Mod. Phys.* **2009**, *81*, 109–162.
6. Medina, H.; Lin, Y. C.; Jin, C.; Lu, C. C.; Yeh, C. H.; Huang, K. P.; Suenaga, K.; Robertson, J.; Chiu, P. W. Metal-Free Growth of Nanographene on Silicon Oxides for Transparent Conducting Applications. *Adv. Funct. Mater.* **2012**, *22*, 2123–2128.
7. Lu, C. C.; Lin, Y. C.; Yeh, C. H.; Huang, J. C; Chiu, P. W. High Mobility Flexible Graphene Field-Effect Transistors with Self-Healing Gate Dielectrics. *ACS nano* **2012**, *6*, 4469–4474.
8. Lui, C. H.; Li, Z.; Mak, K. F.; Cappelluti, E.; Heinz, T. F. Observation of an Electrically Tunable Band Gap in Trilayer Graphene. *Nat. Phys.* **2011**, *7*, 944–947.
9. Lopes dos Santos, J. M. B.; Peres, N. M. R.; Castro Neto, A. H. Graphene Bilayer with a Twist: Electronic Structure. *Phys. Rev. Lett.* **2007**, *99*, 256802.
10. Shallcross, S.; Sharma, S.; Kandelaki, E.; Pankratov, O. A. Electronic Structure of Turbostratic Graphene. *Phys. Rev. B.* **2010**, *81*, 165105.
11. Li, G.; Luican, A.; Lopes dos Santos, J. M. B.; Castro Neto, A. H.; Reina, A.; Kong, J.; Andrei, E. Y. Observation of van Hove Singularities in Twisted Graphene Layers. *Nat. Phys.* **2010**, *6*, 109–113.
12. Lee, D. S.; Riedl, C.; Beringer, T.; Castro Neto, A. H.; von Klitzing, K.; Starke, U.; Smet, J. H. Quantum Hall Effect in Twisted Bilayer Graphene. *Phys. Rev. Lett.* **2011**, *107*, 216602.
13. Ohta, T.; Bostwick, A.; Seyller, T.; Horn, K.; Rotenberg, E. Controlling the Electronic Structure of Bilayer Graphene. *Science* **2006**, *313*, 951–954.
14. Castro, E. V.; Novoselov, K. S.; Morozov, S. V.; Peres, N. M. R.; Lopes dos Santos, J. M. B.; Nilsson, J.; Guinea, F.; Geim, A. K.; Castro Neto, A. H. Biased Bilayer Graphene: Semiconductor with a Gap Tunable by the Electric Field Effect. *Phys. Rev. Lett.* **2007**, *99*, 216802.
15. Oostinga, J. B.; Heersche, H. B.; Liu, X. L.; Morpurgo, A. F.; Vandersypen, L. M. K. Gate-Induced Insulating State in Bilayer Graphene Devices. *Nat. Mater.* **2008**, *7*, 151–157.
16. Luican, A.; Li, G.; Reina, A.; Kong, J.; Nair, R. R.; Novoselov, K. S.; Geim, A. K.; Andrei, E. Y. Single-Layer Behavior and Its Breakdown in Twisted Graphene Layers. *Phys. Rev. Lett.* **2011**, *106*, 126802.
17. Wang, Z. F.; Liu, F.; Chou, M. Y. Fractal Landau-Level Spectra in Twisted Bilayer Graphene. *Nano Lett.* **2012**, *12*, 3833–3838.
18. Hass, J.; Varchon, F.; Millán-Otoya, J. E.; Sprinkle, M.; Sharma, N.; de Heer, W. A.; Berger, C.; First, P. N.; Magaud, L.; Conrad, E. H. Why Multilayer Graphene on 4H-SiC-(000−1) Behaves Like a Single Sheet of Graphene. *Phys. Rev. Lett.* **2008**, *100*, 125504.
19. Sprinkle, M.; Hicks, J.; Tejeda, A.; Taleb-Ibrahimi, A.; Le Fèvre, P.; Bertran, F.; Tinkey, H.; Clark, M. C.; Soukiassian, P.; Martinotti, D.; *et al.* Multilayer Epitaxial Graphene Grown on the SiC(000−1) Surface; Structure and Electronic Properties. *J. Phys. D: Appl. Phys.* **2010**, *43*, 374006.
20. Kim, K.; Coh, S.; Tan, L. Z.; Regan, W.; Yuk, J. M.; Chatterjee, E.; Crommie, M. F.; Cohen, M. L.; Louie, S. T.; Zettl, A. Raman Spectroscopy Study of Rotated Double-Layer Graphene: Misorientation-Angle Dependence of Electronic Structure. *Phys. Rev. Lett.* **2012**, *108*, 246103.
21. Carozo, V.; Almeida, C. M.; Ferreira, E. H. M.; Cançado, L. G.; Achete, C. A.; Jorio, A. Raman Signature of Graphene Superlattices. *Nano Lett.* **2011**, *11*, 4527–4534.
22. Lin, Y. C.; Jin, C.; Lee, J. C.; Jen, S. F.; Suenaga, K.; Chiu, P.W. Clean Transfer of Graphene for Isolation and Suspension. *ACS Nano* **2011**, *5*, 2362–2368.
23. Lin, Y. C.; Lu, C. C.; Yeh, C. H.; Jin, C.; Suenaga, K.; Chiu, P.W. Graphene Annealing: How Clean Can It Be? *Nano Lett.* **2012**, *12*, 414–419.
24. Sutter, P. W.; Flege, J. I.; Sutter, E. A. Epitaxial Graphene on Ruthenium. *Nat. Mater.* **2008**, *7*, 406–411.
25. Reina, A.; Jia, X.; Ho, J.; Nezich, D.; Son, H.; Bulovic, V.; Dresselhaus, M. S.; Kong, J. Large Area, Few-Layer Graphene Films on Arbitrary Substrates by Chemical Vapor Deposition. *Nano Lett.* **2009**, *9*, 30–35.
26. Lu, C. C.; Jin, C.; Lin, Y. C.; Huang, C. R.; Suenaga, K.; Chiu, P. W. Characterization of Graphene Grown on Bulk and Thin Film Nickel. *Langmuir* **2011**, *27*, 13748–13753.
27. Li, X.; Cai, W.; An, J.; Kim, S.; Nah, J.; Yang, D.; Piner, R.; Velamakanni, A.; Jung, I.; Tutuc, E.; *et al.* Large-Area Synthesis of High-Quality and Uniform Graphene Films on Copper Foils. *Science* **2009**, *324*, 1312–1314.
28. Li, X.; Magnuson, C. W.; Venugopal, A.; Tromp, R. M.; Hannon, J. B.; Vogel, E. M.; Colombo, L.; Ruoff, R. S. Large-Area Graphene Single Crystals Grown by Low-Pressure Chemical Vapor Deposition of Methane on Copper. *J. Am. Chem. Soc.* **2011**, *133*, 2816–2819.
29. Gao, L.; Ren, W.; Xu, H.; Jin, L.; Wang, Z.; Ma, T.; Ma, L. P.; Zhang, Z.; Fu, Q.; Peng, L. M.; *et al.* Repeated Growth and Bubbling Transfer of Graphene with Millimetre-Size Single-Crystal Grains Using Platinum. *Nat. Commun.* **2012**, *3*, 699.
30. Pan, Y.; Zhang, H.; Shi, D.; Sun, J.; Du, S.; Liu, F.; Gao, H. J. Highly Ordered, Millimeter-Scale, Continuous, Single-Crystalline Graphene Monolayer Formed on Ru (0001). *Adv. Mater.* **2009**, *21*, 2777–2780.
31. Lee, S.; Lee, K.; Zhong, Z. H. Wafer Scale Homogeneous Bilayer Graphene Films by Chemical Vapor Deposition. *Nano Lett.* **2010**, *10*, 4702–4707.
32. Robertson, A. W.; Warner, J. H. Hexagonal Single Crystal Domains of Few-Layer Graphene on Copper Foils. *Nano Lett.* **2011**, *11*, 1182–1189.

33. Yu, Q.; Jauregui, L. A.; Wu, W.; Colby, R.; Tian, J.; Su, Z.; Cao, H.; Liu, Z.; Pandey, D.; Wei, D.; *et al*. Control and Characterization of Individual Grains and Grain Boundaries in Graphene Grown by Chemical Vapor Deposition. *Nat. Mater.* **2011**, *10*, 443–449.
34. Wu, W.; Jauregui, L. A.; Su, Z.; Liu, Z.; Bao, J.; Chen, Y. P.; Yu, Q. Growth of Single Crystal Graphene Arrays by Locally Controlling Nucleation on Polycrystalline Cu Using Chemical Vapor Deposition. *Adv. Mater.* **2011**, *23*, 4898–4903.
35. Kim, H.; Mattevi, C.; Calvo, M. R.; Oberg, J. C.; Artiglia, L.; Agnoli, S.; Hirjibehedin, C. F.; Chhowalla, M.; Saiz, E. Activation Energy Paths for Graphene Nucleation and Growth on Cu. *ACS Nano* **2012**, *6*, 3614–3623.
36. Wofford, J. M.; Nie, S.; McCarty, K. F.; Bartelt, N. C.; Dubon, O. D. Graphene Islands on Cu Foils: The Interplay between Shape, Orientation, and Defects. *Nano Lett.* **2010**, *10*, 4890–4896.
37. Horiuchi, S.; Gotou, T.; Fujiwara, M.; Sotoaka, R.; Hirata, M.; Kimoto, K.; Asaka, T.; Yokosawa, T.; Matsui, Y.; Watanabe, W.; *et al*. Carbon Nanofilm with a New Structure and Property. *Jpn. J. Appl. Phys.* **2003**, *42*, L1073–L1076.
38. Hernandez, Y.; Nicolosi, V.; Lotya, M.; Blighe, F. M.; Sun, Z.; De, S.; McGovern, I. T.; Holland, B.; Byrne, M.; Gun'Ko, Y. K.; *et al*. High-Yield Production of Graphene by Liquid-Phase Exfoliation of Graphite. *Nat. Nanotechnol.* **2008**, *7*, 406–411.
39. Liu, Z.; Suenaga, K.; Harris, P. J. F.; Iijima, S. Open and Closed Edges of Graphene Layers. *Phys. Rev. Lett.* **2009**, *102*, 015501.
40. Trambly de Laissardiére, G.; Mayou, D.; Magaud, L. Localization of Dirac Electrons in Rotated Graphene Bilayers. *Nano Lett.* **2010**, *10*, 804–808.
41. Havener, R. W.; Zhuang, H.; Brown, L.; Hennig, R. G.; Park, J. Angle-Resolved Raman Imaging of Interlayer Rotations and Interactions in Twisted Bilayer Graphene. *Nano Lett.* **2012**, *12*, 3162–3167.
42. Ni, Z.; Liu, L.; Wang, Y.; Zheng, Z.; Li, L. J.; Yu, T.; Shen, Z. G-band Raman Double Resonance in Twisted Bilayer Graphene: Evidence of Band Splitting and Folding. *Phys. Rev. B.* **2011**, *80*, 125404.
43. Wang, Y.; Ni, Z.; Liu, L.; Liu, Y.; Cong, C.; Yu, T.; Wang, X.; Shen, D.; Shen, Z. Stacking-Dependent Optical Conductivity of Bilayer Graphene. *ACS Nano* **2010**, *4*, 4074–4080.
44. Pimenta, M. A.; Dresselhaus, G.; Dresselhaus, M. S.; Cançado, L. G.; Jorio, A.; Saito, R. Studying Disorder in Graphite-Based Systems by Raman Spectroscopy. *Phys. Chem. Chem. Phys.* **2007**, *9*, 1276–1291.
45. Wang, Y. Y.; Ni, Z. H.; Shen, Z. X.; Wang, H. M.; Wu, Y. H. Interference Enhancement of Raman Signal of Graphene. *Appl. Phys. Lett.* **2008**, *92*, 043121.
46. Ferrari, A.; Meyer, J. C.; Scardaci, V.; Casiraghi, C.; Lazzeri, M.; Mauri, F.; Piscanec, S.; Jiang, D.; Novoselov, K. S.; Roth, S.; *et al*. Raman Spectrum of Graphene and Graphene Layers. *Phys. Rev. Lett.* **2006**, *97*, 187401.
47. Cançado, L. G.; Pimenta, M. A.; Neves, B. R. A.; Dantas, M. S. S.; Jorio, A. Influence of the Atomic Structure on the Raman Spectra of Graphite Edges. *Phys. Rev. Lett.* **2004**, *93*, 247401.
48. Rutter, G. M.; Guisinger, N. P.; Crain, J. N.; First, P. N.; Stroscio, J. A. Edge Structure of Epitaxial Graphene Islands. *Phys. Rev. B* **2010**, *81*, 245408.
49. Tian, J. F.; Cao, H. L.; Wu, W.; Yu, Q.; Chen, Y. P. Direct Imaging of Graphene Edges: Atomic Structure and Electronic Scattering. *Nano Lett.* **2011**, *11*, 3663–3368.